ORIGINAL ARTICLE

Synthesis and characterization of WO_3-doped polyaniline to sense biomarker VOCs of Malaria

P. Jisha[1] · M. S. Suma[2] · M. V. Murugendrappa[3]

Abstract

The major goal of this work is to fabricate a chemiresistive sensor using the properties of nanostructured tungsten trioxide (WO_3) doped polyaniline (PAni) nanocomposite to detect malaria biomarker volatile organic compounds (VOCs). The nanocomposite with a mixed morphology of fibers and rod-shaped particles is synthesized using a chemical polymerization method. The mixed morphology of the particles provided a large surface area and porous structure to the nanocomposite and hence more 'target trap zones' were formed in the sensing layer to produce a drastic change in resistance while sensing a target VOC vapour. The morphological and structural characterization of the nanocomposite was done using FESEM, XRD and FT-IR methods. Electrical and dielectric studies was performed to study the transport properties of the WO_3 doped polyaniline nanocomposite at room temperature. The thermal stability characteristics of the nanocomposite was analyzed using TGA (Thermogravimetric analysis). The sensing studies of the drop casted sensors using the nanocomposites were done and sensing and selectivity characteristics were plotted. The sensor showed good selectivity towards the target VOCs. The sensor with a doping concentration of 15% WO_3 in the polyaniline matrix has shown a better response and recovery towards the malaria biomarkers 3-Carene and α-Pinene. The sensor can be used to develop a handheld portable device for malaria biomarker detection from human breath.

Keywords Malaria · Breath-sensor · Polyaniline · WO_3 · Nanocomposite · 3-Carene · α-Pinene

Introduction

Malaria is still considered to be a critical disease transmitted by the infected Anopheles mosquitoes, especially in sub-Saharan Africa and Southeast Asia (World malaria report 2019 2019). In other parts of the globe even though malaria infection is less, but continuous monitoring and regulation are required to rule out the disease in suspected cases. The early detection of the infection is a critical thing in malaria treatment and thus saving the patient. The conventional malaria detection methods are based on blood smears, which needs sample collection, laboratory facilities, and expert to analyze the infection level. Though rapid diagnostic methods are available for malaria diagnosis, they lack specificity and may provide false-positive results (Moyeh et al. 2019). Plasmodium falciparum, Plasmodium malariae, Plasmodium ovale, and Plasmodium vivax are the major pathogen parasites that cause malaria but Plasmodium falciparum is the most lethal parasite that induces malaria in humans. The drug resistance and genetic polymorphism exhibited by the Plasmodium falciparum have made malaria treatments more complicated and also due to this issue the mortality rates are increased (Menard and Dondorp 2017). So a rapid diagnosis and continuous monitoring of Plasmodium infection are needed to identify malaria in its earlier stage to avoid these issues. Thick film blood smear based microscopic tests are the gold standard for malaria detection, but it requires an expert analyst to perform the analysis and not suitable for endemic field tests. Invasive techniques like Rapid diagnostic tests (RDTs), Serological tests, and Molecular–biological techniques are the other methods available for malaria diagnosis but they are costly, not appropriate for acute infection level, and need sophisticated equipment (Tangpukdee et al.

✉ P. Jisha
  jishap@bmsce.ac.in

1. Department of Electronics and Communication Engineering, B.M.S. College of Engineering, Bangalore, India

2. Department of Medical Electronics, B.M.S. College of Engineering, Bangalore, India

3. Department of Physics, B.M.S. College of Engineering, Bangalore, India

2009). Non-invasive methods for diagnosing malaria are acquiring wider interest, because the standardized methods of malaria detection are not suitable for field tests in endemic sites and safety issues with the blood samples. Most of the non-invasive malaria diagnosing techniques are based on breath, urine, and saliva as the biomarkers but these methods still need further optimization to obtain higher accuracy and sensitivity (Amir et al. 2018). Breath is a doubtless biomarker for malaria, since the malaria patient's breath print reveals the presence of some specific VOCs in comparison to a normal human breath. Research works have shown that there are four thioethers are associated with Plasmodium falciparum infection and these are not found to be associated with any other diseases (Berna et al. 2015). The study on the cultures plasmodium falciparum shown that these parasites follow metabolic pathways similar to plant and produce VOCs with a specific odour like terpenes, which will act as mosquito vector attractant and the parasite use this for transmission from one host to another (Kelly et al. 2015). A recent study using thermal desorption and gas chromatography–mass spectrometry (GC–MS) on the breath print of malaria infected children has shown that the breath of infected patients contains six distinct compounds and higher levels of monoterpenes like α-Pinene and 3-Carene, which are mosquito attractants (Schaber et al. 2018). These terpene levels were highly correlated with the plasmodium infection levels, so the identification of these VOCs from the breath of a patient can be used for breath analysis based malaria diagnosis. The effective sensing of the malaria biomarker VOCs from human breath using sensors can offer a non-invasive, low cost, and rapid malaria diagnosis. The major detection techniques available for the biomarker terpenes like α-Pinene and 3-Carene are High-Performance Liquid Chromatography (HPLC), GC–MS, Quartz Crystal Microbalance (QCM) or resistive type sensors using Molecular Imprinted Polymers (MIP) (Lee 2015). A MIP based sensor with interdigitated electrodes have shown better selectivity and sensitivity for terpenes like α-Pinene, 3-Carene, Cedrene and γ-Terpene and shows that polymer-based materials have better affinity towards aromatic VOCs compared to metal oxide semiconductor sensors (Hawari et al. 2013). A review on the chemical sensors has shown that only a few types of equipment like Ion Mobility Spectrometers (IMS), portable mass spectrometers, and portable gas chromatographs could detect the ppb levels of VOC concentration but these are not low-cost devices. And this work revealed that one of the most simple and robust chemical sensor VOC detection is absorption-based polymer Chemiresistive sensors (Ho and Laboratories 2015). The sensing layer in conducting polymer-based Chemiresistive sensor is coated over a pair of electrodes or an array of electrodes, which is the robust and simple form of transduction unit of absorption based sensors (Baharuddin et al. 2019). The sensing material used in

this type of sensors can be inorganic compounds like metal oxides or organic materials like polymers, graphene, and carbon nanotubes, and their resistance will increase or decrease in contact with a target gas or analyte (Huang et al. 2018).

The room temperature sensing of the target VOCs are achieved using organic materials like conducting polymers, while the sensing using metal oxide semiconductor material-based sensors requires complex micro heaters with high power consumption to enable the sensing mechanism (Hua 2014; Jin et al. 2016). A study on the detection of complete VOCs in indoor air has shown that WO_3, SnO_2, ZnO, and In_2O_3 have a better sensing characteristics towards VOCs compared to any other metal oxide variants (Kadosaki et al. 2010). Also, the same work has shown that the sensing response of WO_3, SnO_2 towards aromatic VOCs like terpenes were very high at the optimum temperature of 300°–350 °C but ppb level detection of VOCs were not achieved and high-temperature operation can cause instability. The conducting polymers like polyaniline, polythiophene, and polypyrrole are generally used for building Chemiresistive sensors for room temperature sensing of various VOCs due to their good sensitivity and short response and recovery time (Park et al. 2017). A research work done for the detection of VOCs emitted by plants using polymer-based sensors revealed that polyaniline has a unique ability to sense terpenes emitted due to phytochemical reactions (Weerakoon et al. 2012). A nanocomposite prepared with polyaniline as a matrix and suitable metal oxide as a filler can complement each other so that a stable and highly sensitive VOC sensor operating at room temperature can be achieved (Sen et al. 2016). The conducting polymers like polyaniline offer very good opportunities to use as transduction elements in many biosensors due to their superior operating characteristics. Conducting polymer-based sensing materials exhibit features like simple synthesis procedures, room temperature sensing of various analytes, good electrical conductivity, and tunable specific analyte selectivity by forming composites with other filler materials and ability to sense in the form of microstructured thin films (Aronggaowa et al. 2013). These diverse properties makes conducting polymer a suitable candidate for biosensors and chemical sensors in the areas like nanotechnology. Among various conducting polymers, polyaniline got better environmental stability and tunable electrical properties through doping elements (Sanches et al. 2011). Polyaniline is a conjugated polymer that is generally found in two forms, insulator type emeraldine base form and emeraldine salt form with good conductivity and suitable for sensor applications. The basic chemical structure of the emeraldine salt form of polyaniline is shown in Fig. 1. The conductivity can be significantly altered using protonic acid doping of the polyaniline, because the protonation results in the generation of polarons that will aid in electrical conduction and thereby

Fig. 1 Structure of polyaniline emeraldine salt using nitric acid for protonation
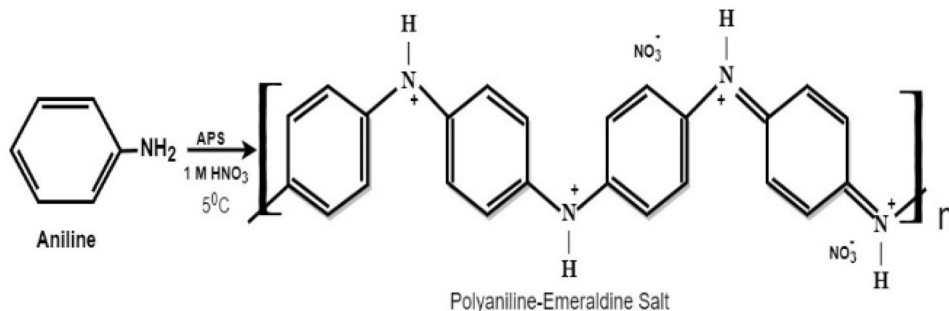
improves the conductivity. Doping with nitric (HNO_3) acid shows a lower resistance and better conductivity (B et al. 2010). Nanostructured polyaniline synthesized through protonic acid doping shows a better selectivity and sensitivity towards analyte molecules (Alfano et al. 2015).

In the literature no research has been reported to detect malaria using the breath marker VOCs. So this paper presents a novel method to detect malaria biomarkers using a conducting polymer-based chemiresistive sensor at room temperature. In this work, a nanomaterial-based chemiresistive sensor to detect malaria biomarker VOCs is prepared using a polyaniline-WO_3 nanocomposite, and sensing characteristics were analyzed. The graphical representation of the proposed system is shown in Fig. 2. The polyaniline-WO_3 nanocomposite was prepared through chemical polymerization method and the morphological and electrical characterization were analyzed. The sensing layer was coated on an FR4 substrate with inter-digitated electrodes using drop-casting method. The basic mechanism of sensing through absorption of target gas is a redox reaction and due to that, the resistance of the sensing material is found to be increasing when exposed to the target vapours. The sensor response curve shows a rapid response and recovery towards α-Pinene and 3-Carene, the biomarker VOCs of malaria.

Also, it exhibited a very good selectivity towards the target VOCs. The developed sensor can be incorporated with a microcontroller unit to develop a portable Malaria sensing device.
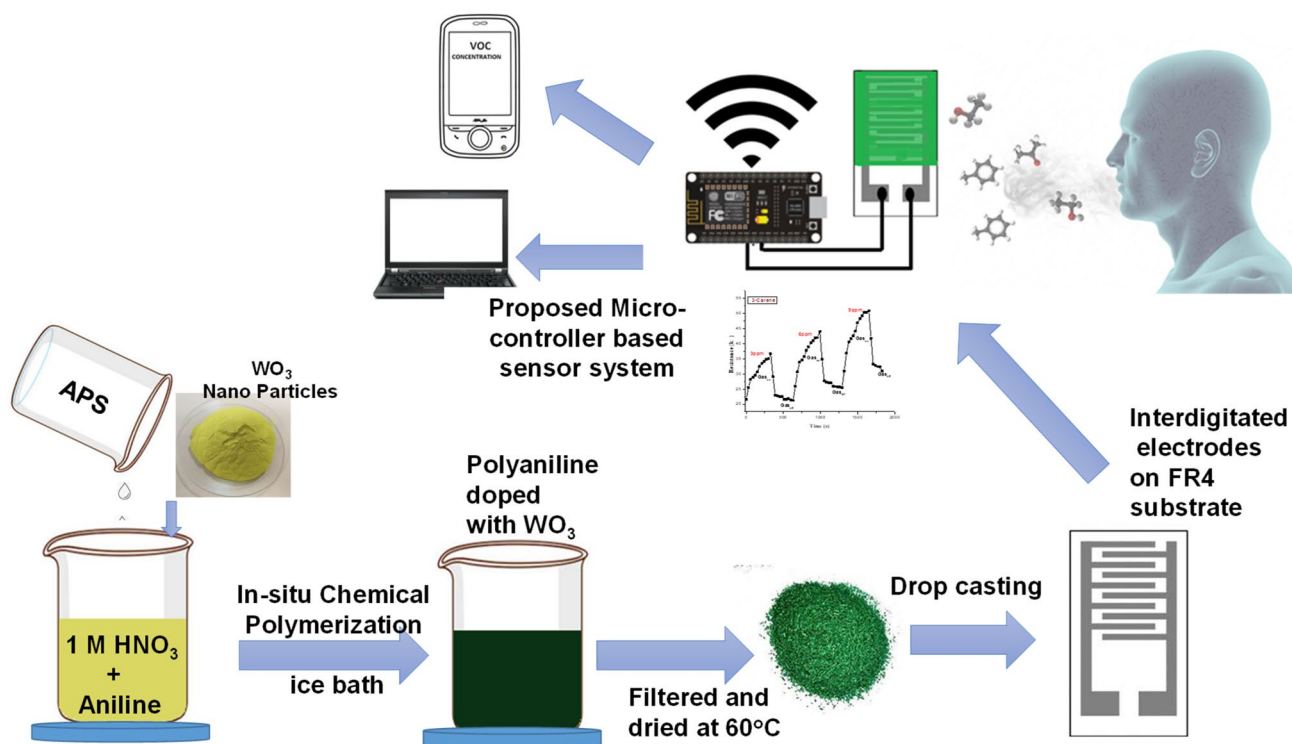

Fig. 2 Schematic representation of WO_3 doped polyaniline synthesis and its sensing application

Materials and methods

Reagents

Aniline, Ammonium persulphate as an oxidizing agent, WO_3 nanoparticles, and Polyvinylidene difluoride (PVDF) were purchased from Sigma Aldrich. Concentrated HNO_3 acid was used as the doping agent. *N*-Methyl-2-Pyrrolidone (NMP) purchased from Sigma Aldrich is utilized for the deposition of sensing material on the FR4 substrate in thick film form. Double distilled water was used for preparing all solutions. All reagents were used without any additional purification. The VOCs to be detected, 3-Carene and α-Pinene were purchased from TCI Chemicals (India) Pvt. Ltd. Protonated polyaniline emeraldine salt synthesized is doped with WO_3 nanoparticles in different weight percentages of 5%, 10%, 15%, and 20% to make polyaniline-WO_3 nanocomposites.

Sensor fabrication

Thick films of WO_3 doped polyaniline emeraldine salt were made on the FR4 substrate, of $1cm^2$ area with interdigitated copper electrodes, using drop-casting method. The electrode patterns were designed using CST Microwave Studio software and patterned by chemical etching. Acetone and de-ionized water are used for the cleaning of the substrate before applying the coatings. The material preparation for film making was done by adding WO_3 doped polyaniline nanocomposite with PVDF, as a binding agent, in a 1:5 ratio and mixing it with 0.2 ml of NMP. The mixed composite used to drop cast on the substrate for thick film sensor preparation and after making the coating on the FR4 substrate with interdigitated copper electrodes attached, the sensors were heated at 60 °C in a hot air oven for drying and removing the NMP content. The electrode bonding pad portion was masked while making the drop-casting. Sufficient and equal lengths of thin Cu wires were attached to the sensor as the electrical contact leads. The resistance variations on exposure to the VOCs were measured and recorded using a 6.5 digit multimeter. The sensors were deployed for sensing the two target VOC vapours, α-Pinene and 3-Carene, in three different concentrations of 3 ppm, 6 ppm, and 9 ppm.

Methods

The morphological and structural characterization of polyaniline-WO_3 nanocomposites was made using JEOL JSM-7100F Field Emission Scanning Electron Microscope (FESEM), XRD on XPERT-3 X-ray diffractometer and FTIR with PerkinElmer FTIR spectrometer in KBr medium. The electrical characterizations of the nanocomposite were made through AC conductivity measurements using Wyne Kerr 6500B Precision Impedance Analyzer at frequencies 100 Hz to 5 MHz and DC conductivity measurements were made using Keithley 6221 current source-nano voltmeter arrangement. Conductivity studies were conducted on pellets of diameter 13 mm and a thickness of 1.6 mm made using a hydraulic press by applying 5–7 tons of pressure. To analyze and study the conductivity and dielectric properties of the prepared polyaniline-WO_3 nanocomposite, parameters like impedance, phase angle, capacitance, conductance, and dissipation factor are recorded at room temperature. The thermal decomposition of polyaniline-WO_3 nanocomposites with different filler concentrations studied through thermogravimetric analysis using TGA-DTA Perkin Elmer STA6000. TGA of HNO_3 doped polyaniline and its WO_3 doped polyaniline nanocomposite was conducted with a temperature variation from 40° to 800 °C using Nitrogen as the initial purge gas and with a heating rate of 20 °C/ min. The electrical resistance variation of the sensing layer upon exposing the target vapours are measured using Picotest M3510A-6 ½ digit multimeter by applying two probe method. The FR4 substrate of 0.5 mm thickness, attached with an interdigitated copper electrode array made of electrode fingers with 0.1 μm thickness, 0.3 mm width, and 6 mm length was used as the sensing element. Drop casting is used to make a thick film of the sensing layer on the FR4 substrate. Using polyaniline nanocomposites of different weight percentages on FR4 substrates, five sensing elements were fabricated and sensing studies were made.

Results and discussion

Morphological characterization of polyaniline-WO_3 nanocomposite

The surface morphology of the synthesized polyaniline-WO_3 nanocomposite is analyzed by Field Emission Scanning Electron Microscope (FESEM) with Energy Dispersive X-Ray Spectroscopy (EDAX). The composite has a mixed morphology consisting of a heterogeneous mixture of agglomerated particles of rod, sheet, and fibrous shapes. The WO_3 particles are non-uniformly distributed over an agglomerated sheet-like formation of the polymer matrix. The protonic acid doped polyaniline has got a rod shape agglomerated morphology. In the polyaniline-WO_3 nanocomposites with 5% and 10% doping concentration, the presence of WO_3 particles was non-uniform and tightly clustered in nature. The 15% and 20% doping concentration composites have more loosely bound WO_3 particles present inside and outside the sheet-like matrix. The nanocomposite with 20% doping concentration was found to be of more

crystalline in nature than amorphous, unlike the other three nanocomposites. FESEM images of polyaniline-WO_3 nanocomposites shown in Fig. 3a–f revealed that the composite consists of particle sizes of less than 20 nm stacked upon each other to form a sheet-like morphology. The randomly distributed particles are found to be agglomerated and formed clusters. This random non-uniform distribution of particles has introduced some vacant spaces, called pores, between the clusters which aids in the sensing behavior of the material. The Energy Dispersive X-Ray Spectroscopy confirm the presence of Tungsten in the polyaniline-WO_3 nanocomposites and a gradual increase in weight percentage was visible in the mapping reports as shown in Fig. 4.

Structural characterization of polyaniline-WO_3 nanocomposite using XRD analysis

The structure of the polymer composite prepared was made by powder method of X-ray diffraction on XPERT-3 X-ray diffractometer with Cu Kα-radiation ($\lambda = 1.54060$ Å), 2θ range from 10° to 80° and step size [2θ] = 0.0300 per 0.8 s. Figure 5 shows the X-ray diffractogram of the polyaniline-WO_3 nanocomposite, doped with 5%, 10%, 15%, and 20% of WO_3 nanoparticles.

The XRD peaks obtained in the spectrum of WO_3 nanoparticles are in agreement with the standard (h k l) planes, ensures that the synthesized material contains monoclinic WO_3 structure (ICDD DATA CARD 98-001-5905). All the significant diffraction peaks are corresponding to (100), (020), (002), (02−1), (111), (120), (02−2), (10−2), (12−2), (004), (211) and (12−4) crystal planes. Determined values of lattice constants of polyaniline-WO_3 nanocomposite are found to be $a = 3.8317$ Å, $b = 7.50573$ Å and $c = 7.256609$ Å, which are exceptionally near to the reported values of WO_3 (ICDD DATA CARD 98-001-5905). The average crystallite size determined using Scherer's formula for WO_3 nanoparticles is ~25 nm. Also, from the polyaniline-WO_3 nanocomposite XRD pattern, the peaks corresponding to WO_3 nanoparticles are visible. But there is a small shift in the standard peak positions due to the occurrence of polyaniline matrix. The intensity of the major peaks are reduced and broadened in the composite in comparison to the pure WO_3 nanoparticles. The broadened crystalline peaks in the composite represent reduced crystalline size of the particles. The observed full-width half-maximum (FWHM, β) is decreasing slightly with an increase in weight percentage of WO_3. The crystallite size can be computed using Debye–Scherrer's formula and the doping concentration of metal oxide is a significant parameter impacting the
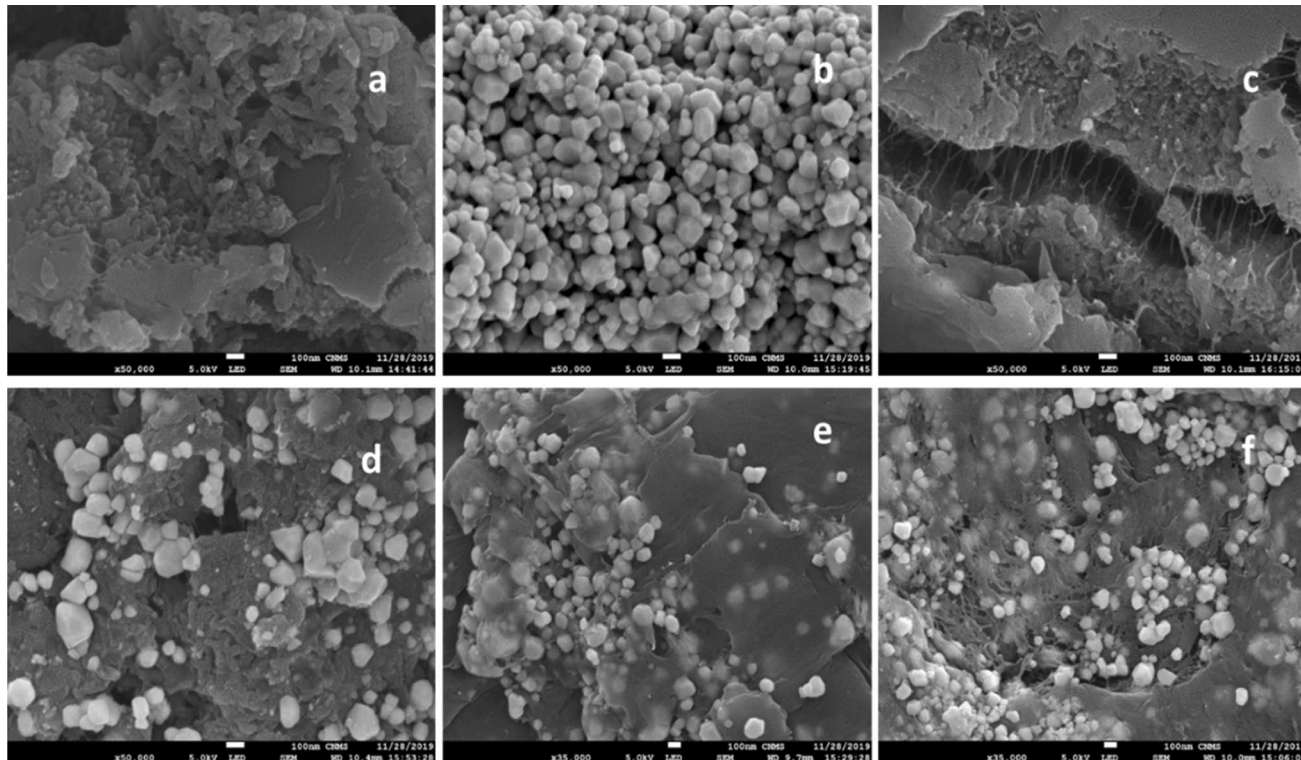

Fig. 3 FESEM: **a** HNO_3 doped PAni, **b** WO_3 nano particles, **c** PAni—HNO_3/WO_3-5%, **d** PAni—HNO_3/WO_3-10%, **e** PAni—HNO_3/WO_3-15%, **f** PAni—HNO_3/WO_3-20%
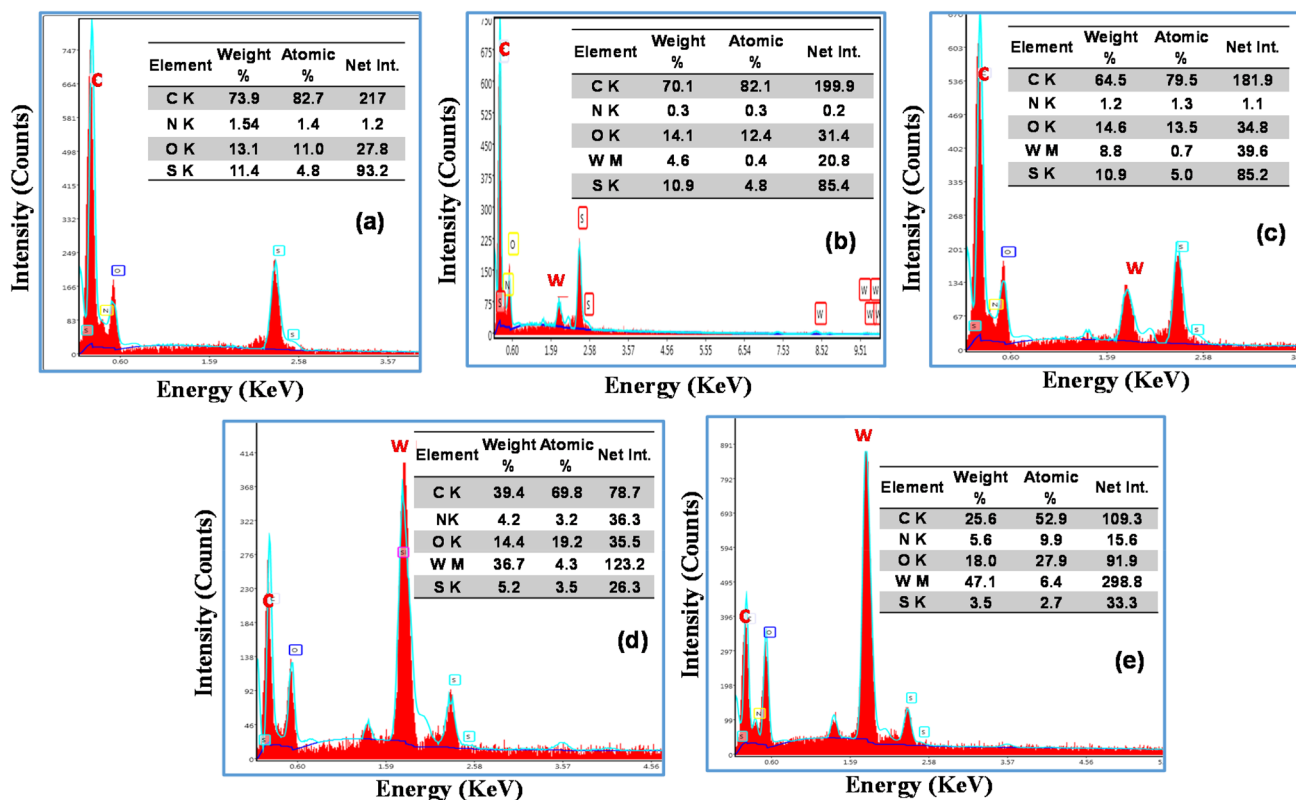
Fig. 4 EDAX: **a** HNO$_3$ doped PAni, **b** PAni—HNO$_3$/WO$_3$-5%, **c** PAni—HNO$_3$/WO$_3$-10%, **d** PAni—HNO$_3$/WO$_3$-15%, **e** PAni—HNO$_3$/WO$_3$-20%
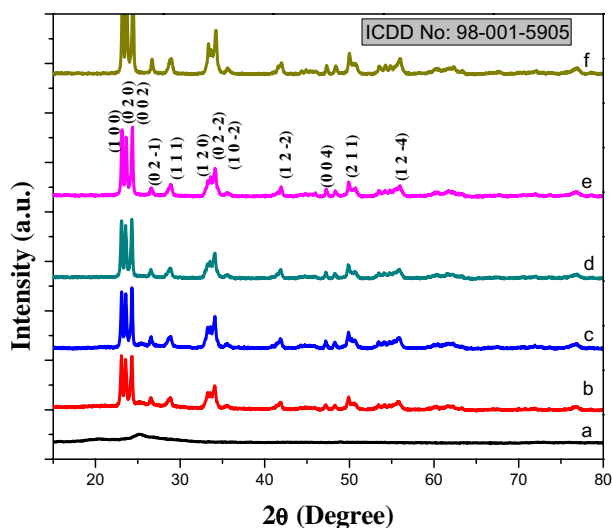
Fig. 5 XRD: **a** HNO$_3$ doped PAni, **b** PAni—HNO$_3$/WO$_3$-5%, **c** PAni—HNO$_3$/WO$_3$-10%, **d** PAni—HNO$_3$/WO$_3$-15%, **e** PAni—HNO$_3$/WO$_3$-20%, **f** WO$_3$ nanoparticles

composite crystallinity of the nanocomposite (Gomathi et al. 2018). The average nano crystallite size is calculated using Debye–Scherrer's formula:

$$D = \frac{K\lambda}{\beta \cos\theta}, \tag{1}$$

where D represents the crystallite size, K corresponds to the shape factor (0.9), and λ is the wavelength of K-alpha radiation, β is the full-width half-maximum at Bragg's angle 2θ. Using this equation the average crystallite size of the polyaniline composite doped with 5%, 10%, 15%, and 20% of WO$_3$ nanoparticles are calculated and found to be nearly 18 nm, 19 nm, 20 nm, and 21 nm, respectively. The crystal symmetry defects are mainly due to lattice strain which is an indication of both defects and dislocation. The strain is the reason behind lattice deformation which results in the excess stress in the crystal matrix. Also, the lattice strain leads to peak widening in the XRD spectra. Assume, lattice strain, and crystallite size are contributing independently to the line broadening, the strain produced in the polyaniline-WO$_3$ nanocomposite crystalline structure can be calculated using Williamson–Hall (W–H) relation (Mote et al. 2012):

$$\varepsilon = \frac{\beta_{hkl}}{4\tan\theta}, \tag{2}$$

where 'ε' lattice strain produced in the crystalline particles and 'β' is the full-width half-maximum at Bragg's angle 2θ.

W–H analysis is used for the evaluation of crystallite size calculation or lattice strain measurement using various models like uniform deformation model, uniform deformation stress model or uniform deformation energy density model. From Debye–Scherrer's formula (1) and Williamson–Hall (W–H) relation (2), it can be observed that the peak width depends on the factor $1/\cos\theta$ and strain depends on the factor $\tan\theta$. Now by considering that the line broadening due to crystallite size and strain are independent of each other, then we get the W–H equation as

$$\beta \cos \theta = \frac{K\lambda}{D} + 4\varepsilon \sin \theta. \tag{3}$$

W–H graphical analysis uses a liner fit in a plot drawn with $\beta\cos\theta$ on Y axis and $4\sin\theta$ on X axis to calculate the crystallite size and micro strain from the Y intercept and the slope of the fit, respectively. The average lattice strain calculated using W–H equation for the composite prepared is 8.74×10^{-3}, which is approximately equal to the strain value obtained from the Williamson–Hall graphical method as shown in Fig. 6.

The dislocation density (δ) is defined as the length of dislocation lines per unit volume of the crystal and can be computed using Williamson–Smallman relation (Devi et al. 2019):

$$\text{Dislocation density, } \delta = \frac{1}{D^2}, \tag{4}$$

where D is the crystallite size of the polyaniline-WO$_3$ nanocomposite determined using the Scherrer's formula.

The interchain separation length (R) of the nanocomposite synthesized is calculated using the formula (4) given below (Du et al. 2014). The R value corresponding to the major peaks in the XRD pattern of the composites have been calculated and listed in Table 1. The composite which has the shortest R value will have higher conductivity, since when the interchain separation decreases, the possibility of interchain hopping of charge carriers increases:

$$R = \frac{5\lambda}{8\sin\theta}. \tag{5}$$

In polyaniline nanocomposites, amorphous areas are non-conducting in nature, while the crystalline regions are more conducting in nature. So the conductivity is directly proportional to crystallinity. Also if the d-spacing and interchain separation decreases there will be an increase in interchain hopping, which in turn causes an increase in conductivity (Bhadra and Lee 2009). The polyaniline protonated using nitric acid has higher values of strain, dislocation density, d-spacing, and interchain separation compared to WO$_3$ doped polyaniline. Also, these parameters were found to be decreasing when the doping concentration increases. Hence the conductivity of the WO$_3$ doped polyaniline nanocomposite is observed to be higher than that of an un-doped polyaniline sample. The Various XRD parameters calculated for the polyaniline composite doped with different weight percentage of WO$_3$ is shown in Table 1. The crystalline plane and the d-spacing, interchain separation, lattice strain, and dislocation density corresponding to the diffraction peaks identified in Fig. 3 are summarized in Table 2.
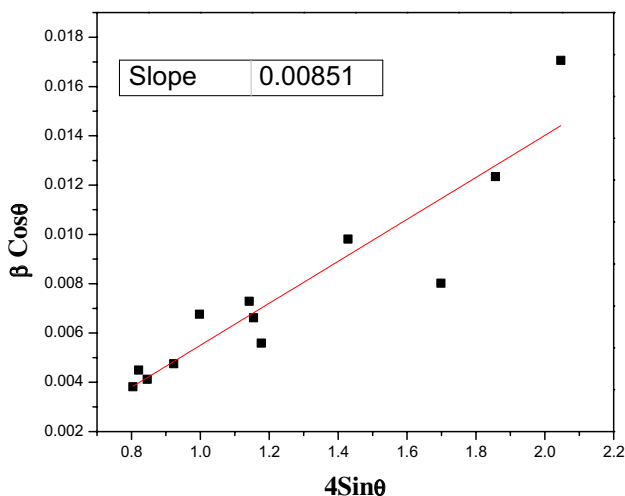

Fig. 6 W–H plot of $\beta\cos\theta$ vs. $4\sin\theta$

Table 1 Various XRD parameters of PANI-WO$_3$ nanocomposites

Materials	Average crystallite size D (nm)	Average crystallite dislocation density (δ)$\times 10^{-3}$ (nm^{-2})	Average Microstrain (ε)*10^{-3}	Average interchain separation length, R	Average d-spacing
HNO$_3$ doped PAni	1.59	465.13	114.74	0.5005	4.0040
PAni—HNO$_3$/WO$_3$-5%	18.53	14.55	8.71	0.2876	2.3010
PAni—HNO$_3$/WO$_3$-10%	18.76	13.17	7.92	0.2838	2.2701
PAni—HNO$_3$/WO$_3$-15%	20.44	11.28	6.99	0.2810	2.2483
PAni—HNO$_3$/WO$_3$-20%	20.63	7.25	6.17	0.2809	2.2468

Table 2 Various XRD parameters of PANI-WO$_3$ nanocomposite corresponding to major peaks

Sl. no.	Miller indices (h k l)	Peak (2Theta)	FWHM	Crystallite size D (nm)	Crystallite dislocation density(δ)$\times 10^{15}$ lines/m^2	Micro strain (ε)*10^{-3}	Interchain separation length, R (A^0)	d-spacing (A^0)
1	1 0 0	23.20	0.22	36.34	0.76	4.7446	0.48	3.8317
2	0 2 0	23.69	0.26	30.85	1.05	5.4743	0.47	3.7529
3	0 0 2	24.42	0.24	33.63	0.88	4.8747	0.46	3.6426
4	0 2 −1	26.68	0.28	29.16	1.18	5.1518	0.42	3.3382
5	1 1 1	28.88	0.51	16.13	3.84	8.6167	0.39	3.0894
6	1 2 0	33.17	0.44	19.03	2.76	6.3803	0.34	2.6987
7	1 0 −2	33.54	0.78	10.68	8.77	11.2522	0.33	2.6695
8	0 2 −2	34.22	0.34	24.81	1.62	4.7483	0.33	2.6179
9	1 2 −2	41.85	0.60	14.13	5.01	6.8691	0.27	2.1568
10	0 0 4	50.25	0.99	8.83	12.83	9.2459	0.23	1.8142
11	2 1 1	55.33	2.27	3.95	63.95	18.8807	0.21	1.6592
12	1 2 −4	61.54	2.55	3.63	76.03	18.6826	0.19	1.5056
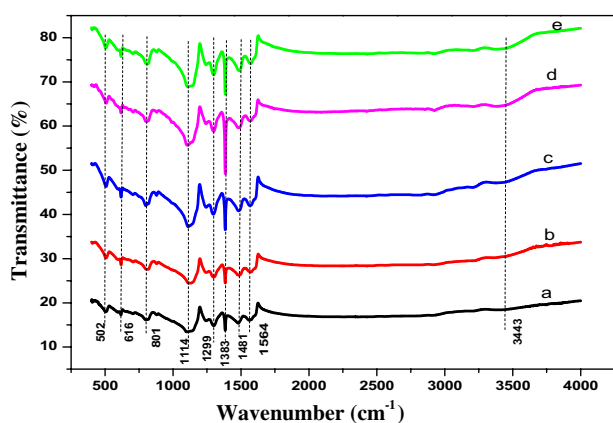
Fig. 7 FTIR spectra: **a** HNO$_3$ doped PAni, **b** PAni—HNO$_3$/WO$_3$-5%, **c** PAni—HNO$_3$/WO$_3$-10%, **d** PAni—HNO$_3$/WO$_3$-15%, **e** PAni—HNO$_3$/WO$_3$-20%

Table 3 Absorption bands of FTIR Spectra of PAni-WO$_3$ nanocomposite and their vibrational assignments

Wavenumber (cm^{-1})	Vibrational assignments
3443	Stretching of (N–H) primary amino group
1564	Quinonoid (Q) ring stretching (The C=C stretching vibration of quinoid)
1481	Benzenoid (B) ring stretching (The C=C stretching vibration of benzoid)
1383	C=C and C–C stretching and bending modes in quinonoid units. Weak C–N stretching absorption in QBQ units
1299	Stretching (C–N) of secondary aromatic amine (The C=N stretching vibration in quinoid)
1114	In-plane bending vibration of QNH+B bond
801	Out of plane bending mode of (C–H) in 1, 4 di-substituted Benzene ring
616	O–W–O stretching mode
502	C–H out-of-plane bending vibration

Fourier-transform infrared spectroscopy (FTIR) analysis

The FTIR spectra of the polyaniline-WO$_3$ nanocomposites were recorded with the PerkinElmer FTIR spectrometer with a wavenumber range of 400–4000 cm^{-1} consisting 32 scans per second. The nanocomposites in powder form and Potassium Bromide (KBr) were grounded together into fine powders and transformed as thin pellets for FTIR analysis. Figure 7 shows the FTIR spectrum of polyaniline-WO$_3$ nanocomposites with different weight% of WO$_3$. The main absorption peaks of the composite prepared are listed in Table 3. In the FTIR absorption spectra of polyaniline nanocomposite doped with different weight% of WO$_3$, the samples have eight major absorption bands that are found to be in the range of 900–1600 cm^{-1}. The absorption peaks

between 1100 and 1200 cm^{-1} are due to the in-plane bending vibration of both Q=NH$^+$−B bond and benzenoid or quinonoid C–H bond (where B represents benzene-type rings and Q corresponds to quinonic-type rings). Absorption peaks at 1564, 1481, and 1114 cm^{-1} in polyaniline emeraldine salt are attributed to a semi quinoid polaron lattice structure (Lee et al. 2012; Kellenberger et al. 2012). Among these bands, the intensity of Q=NH$^+$−B stretching is indicated by the absorption peak at 1114 cm^{-1}, assigned as characteristic absorption band of emeraldine salt, which is strongest. Q=NH$^+$−B bonds are formed through doping polyaniline with H$^+$ through protonic acid doping using strong nitric acid (Trchová and Stejskal 2011; Zou et al. 2014). They are normally considered as polaron or

bipolarons which can create an excitation band in the middle of valence and conduction band. So due to this, polarons play a major role in the electrical conductivity of polyaniline. Among all the nanocomposites prepared, the intensity of $Q=NH^+-B$ in polyaniline doped with 15% of WO_3 has the strongest absorption peak, which confirms that the concentration of polaron or bipolaron in that composite is higher and there may be a greater chance for the higher conductivity for polyaniline-WO_3-15% nanocomposite.

Also, the absorption peak at 1114 cm^{-1} indicates the in-plane bending vibration of the C−H bond of 1,2,4-ring structures. WO_3 FTIR spectrum usually contains a broad absorption peak at characteristic protonic acid doped polyaniline absorption peak at 1114 cm^{-1} in the spectrum (Trchová and Stejskal 2011) of intensities at these peaks can confirm the emeraldine form of polyaniline. The ratio calculated is found to be very close to unity and hence it confirms that polyaniline is in the emeraldine salt form in the composite.

The absorption peaks at 1564 and 1481 cm^{-1} are corresponding to the C=N and C=C stretching mode of vibration for the quinonoid and benzenoid rings of polyaniline (Dhivya et al. 2016). 1383 cm^{-1} is allocated to weak C–N stretching vibration in the bonds near to the quinonoid ring in the FTIR absorption spectra of polyaniline. The absence of the 1364 cm^{-1} band indicates an increase in conductivity and it also indicates a morphology change from ribbons to nanofibers and nanotubes (Kang et al. 1993; Laslau et al. 2009). The peaks at 1299 cm^{-1} correspond to the stretching mode of the C–N bond of secondary amines in the benzenoid ring. The strong band at this peak is due to the C–N bond stretching vibrations in aromatic amines of para-linked aniline units also corresponds delocalization of the π-electron caused in the polymer chain due to protonic acid doping (Trchová and Stejskal 2011).

The FTIR spectra indicate a few bands in the range from 2800 to 4000 cm^{-1} due to NH bond stretching vibrations in the polymer chain. The 3406 cm^{-1} band is corresponding to the stretching vibration of secondary amine (Kang et al. 1993; Dhivya et al. 2016). The stretching mode of O–W–O bond appears as a broadband around 616 cm^{-1} which is close to the absorption peak of WO_3 at 618 cm^{-1} (Zou et al. 2014). The out of plane bending modes of C–H bond in the replacements present in the benzene ring are generally represented by 1000–400 cm^{-1} absorption peak regions. The region 900–700 cm1 corresponds to the aromatic ring and out-of-plane C–H deformation vibrations. The minor absorption peaks at the 801 cm^{-1} spectrum is related to benzene and quinonoid ring deformations. The absorption band present in 502 cm^{-1} is due to the out-of-plane bending vibration of the C−H bond and this can be used to detect the type of substituted benzene (Dhivya et al. 2016). The FTIR spectra of the polyaniline-WO_3 nanocomposites synthesized, show a slight shift in the wavenumbers to higher absorption wavelength regions. The increase of absorption peak wavelength is proportional to the conjugation length decrease in HNO_3 doped polyaniline and HNO_3 doped polyaniline-WO_3 nanocomposites with different doping concentrations of WO_3, which in turn confirms the interaction between the WO_3 nanoparticles and polyaniline matrix. Hence this confirms the formation of polyaniline-WO_3 nanocomposite. The major absorption peaks and their vibrational assignments for the synthesized polyaniline nanocomposite doped with different weight% of WO_3 is listed in Table 3.

Transport studies

AC conductivity

To analyze the charge conduction mechanism in the HNO_3 doped polyaniline-WO_3 nanocomposites, AC conductivity variations concerning frequency variations from 100 Hz to 5 MHz is studied for all compositions at room temperature and the graphical representation is shown in Fig. 8. From the AC conductivity plot, conductivity is independent of frequency at lower frequency regions and almost equal to the DC conductivity value. Also, the AC conductivity is found to be increasing at a higher frequency range because of the charge transport between the protonic acid dopant and the polymer chain, which is the characteristic of disordered materials (Bisquert 2004; Sastry et al. 2013). At lower frequencies, the real part of σ_{AC} becomes equals to the DC conductivity and at higher frequencies, $\sigma_{AC}=A\omega^S$, where A is the area coated with the material and S is the frequency exponential factor which has a value less than or equal to 1 (Bekri-abbes and Srasra 2015). The relationship
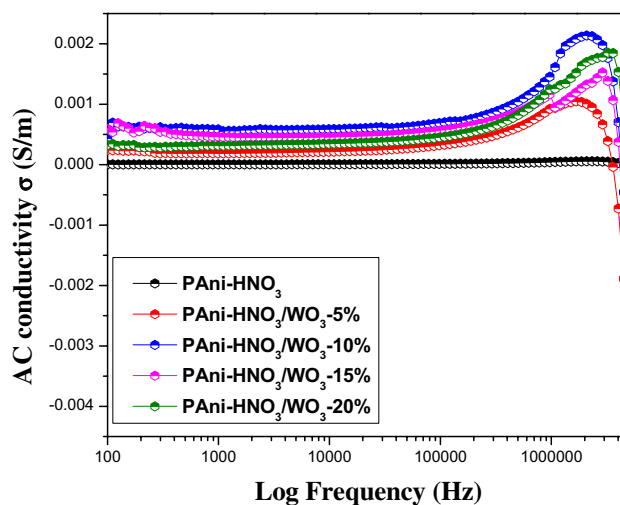

Fig. 8 AC conductivity for frequency variations of PAni—HNO_3/WO_3-5, 10, 15 and 20% nanocomposites

of ac conductivity with frequency is calculated using the following equation:

$$\sigma_{AC} = \varepsilon_0 \varepsilon' \omega \tan \delta. \tag{6}$$

The calculations from XRD of the composites reveals the interchain separation length of the composites. The conductivity values are showing a good agreement with the XRD results, with a high conductivity for the polyaniline-WO_3 nanocomposites in comparison to the HNO_3 acid doped polyaniline due to the reduction in interchain separation length in WO_3 doped composites.

DC conductivity

The change in DC conductivity of the material concerning doping concentration is studied at room temperature and shown in Fig. 9 and it shows the semiconductor behaviour of the polyaniline-WO_3 nanocomposite. The DC conductivity is found to be increasing with an increase in weight percentage of WO_3 up to 15% and then observed as decreasing for 20%-WO_3. This shows that the conductivity variation in the polymer matrix by adding WO_3 filler with a particular weight percentage obeys the theory of percolation threshold. Studies revealed that the DC conductivity of protonic acid doped polymers mainly determined by the morphology and other factors like monomer type, doping concentration, and the amount of crystallinity. The large increase in conductivity doped (protonated) polyaniline is because it acts like a polyelectrolyte, a big molecule with a huge number of ionizable groups. The macromolecular configuration helps to minimize conjugation defects present in the polymer chain structure and aids in linear
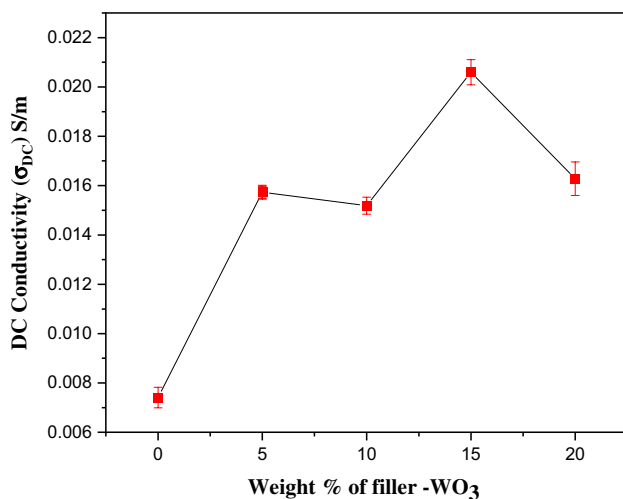
conformation required for crystallization. Hence it results in the crystallinity increment of the polymer composite with an improvement in bulk conductivity (Metals 1994; Kumar 2002). As observed from the FTIR and XRD studies on the polyaniline-WO_3 nanocomposite, there is a visible change in the molecular configuration of the Polyaniline matrix with an increased amount of crystallinity and due to that, an enhancement in the conductivity of composite is achieved. Keithley 6221 current source-nano voltmeter arrangement is used for the I–V characterization of the WO_3 doped polyaniline nanocomposite at room temperature.

The voltage variations corresponding to the variations of current from − 5 mA to + 5 mA are recorded and plotted as shown in Fig. 10. The electrical conductivity is calculated from these current and voltage values using the equation given below:

$$\sigma_{DC} = \frac{1}{\rho}, \tag{7}$$

where the resistivity ρ is computed from the voltage measured for the variations in current values (Qasim et al. 2007).

I—V characteristics show that the ohmic behavior of the protonic acid doped polyaniline is decreasing with an increase in the filler weight percentage. It can be observed that the voltage value corresponding to a particular current is decreasing with an increase in doping concentration up to 15% and beyond that, an increase in voltage value is observed, for polyaniline-WO_3 composite with 20% filler concentration. Hence the maximum conductivity is observed for polyaniline-WO_3 composite with a filler weight percentage of 15% which can be due to its high crystalline properties.
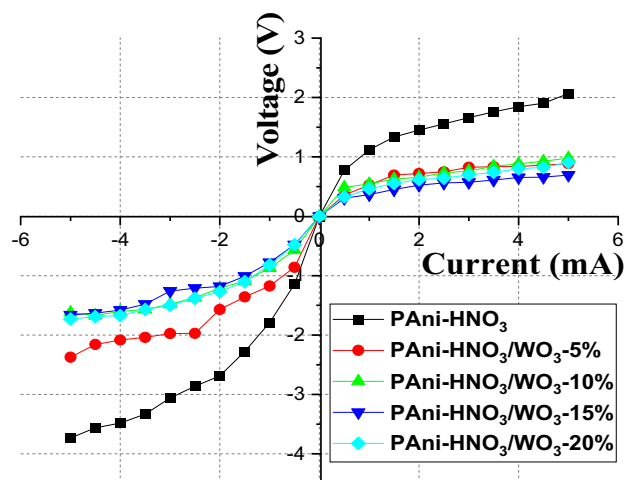

Fig. 9 DC conductivity variations for weight% of WO_3

Fig. 10 I–V characteristics of polyaniline-WO_3 nanocomposites

Fig. 11 Dielectric constant of polyaniline-WO$_3$ nanocomposites
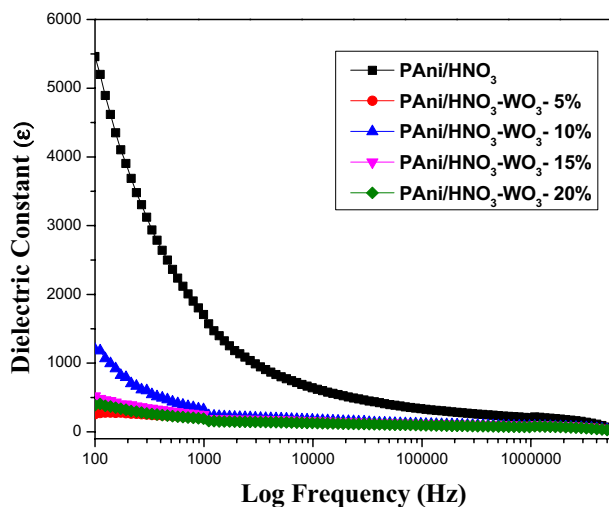

Fig. 12 Dielectric loss of polyaniline-WO$_3$ nanocomposites

Dielectric studies

The changes in dielectric constant (ε) value for frequency variations at room temperature for the polyaniline-WO$_3$ nanocomposite in the frequency range of 100 Hz to 5 MHz is shown in Fig. 11. Nitric acid (HNO$_3$) doped polyaniline has got the maximum value of dielectric constant and followed by the WO$_3$ nanocomposite samples. The dielectric constant follows a reverse variation pattern of conductivity. When the doping concentration of WO$_3$ increases, the dielectric constant decreases. At lower frequencies, the dielectric constant has got the maximum value and it is found to be decreasing with an increase in frequency. The interfacial effects inside the bulk samples or the electrode effects might have contributed to the large values of dielectric constant at lower frequency range. At high frequencies, the ion diffusion in the material cannot follow the direction of quick periodic changes of the applied electric field. So the dielectric constant decreases due to the reduction in charge accumulation based on the polarization (Bekri-abbes and Srasra 2015). Debye type relaxation effect is responsible for the higher value of dielectric constant at low frequency (Cao and Gerhardt 1990). Figure 12 represents the dependence of dielectric loss (tan δ) on frequency for polyaniline-WO$_3$ nanocomposites at room temperature. The dielectric loss is frequency dependent in the case of materials with conductivity and relaxation polarization. The loss factor tan δ decreases with an increase in frequency. The nanocomposites have a lower tan δ response in comparison to the HNO$_3$ doped polyaniline matrix. But the polyaniline composite with a WO$_3$ weight percentage of 15% has shown higher dielectric loss compared to the polyaniline matrix.

The 15% WO$_3$-doped polyaniline nanocomposite has got higher AC and DC conductivity due to its morphological
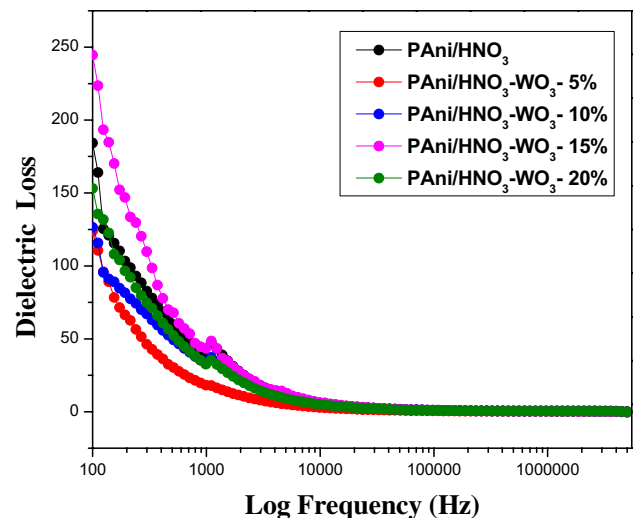
characteristics. So due to the higher conductivity and interfacial relaxation, the dielectric loss associated with the particular nanocomposite has got a higher tan δ response (Kar and Choudhury 2012). The higher value of dielectric constant for the synthesized polyaniline-WO$_3$ nanocomposite makes it suitable for nano devices which require higher conductivity at lower frequencies.

Sensing characteristics

The synthesized polyaniline-WO$_3$ nanocomposites were tested for the room temperature sensing of malaria biomarker VOCs, α-Pinene, and 3-Carene. The sensing studies were carried out inside a test chamber. The nanocomposites to be tested were coated on an FR4 substrate attached with interdigitated copper electrodes for electrical contacts. The CST microwave studio layout design of the sensor is shown in Fig. 13. A known amount of VOCs was allowed to pass to the test chamber, and the resistance variations were recorded for the time of regular intervals using Picotest M3510A-6 ½ digit multimeter, till it reaches a constant value. These steps were performed again for both all the weight% of WO$_3$ filled polyaniline nanocomposites and for different VOC concentrations. The drop cast sensors were tested multiple times at room temperature to ensure the reliability of the output resistance variation.

The response of the sensor towards the target VOCs is calculated using the equation:

$$\text{Sensitivity, } \%S = \frac{R_g - R_a}{R_a} \times 100\% = \frac{\Delta R}{R_a} \times 100\%, \quad (8)$$

where R_g represents the resistance of the sensor in the presence of target VOC vapour and R_a corresponds to the
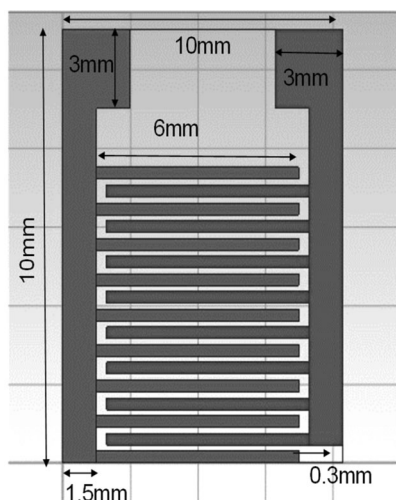
Fig. 13 Layout design of the VOC sensor

Fig. 14 VOC sensing sensitivity of HNO$_3$ doped PAni and PAni—HNO$_3$/WO$_3$ nanocomposite based sensors

resistance of the sensor in the presence of air during initial conditions. The concentration of the liquid analyte taken is assumed to be diffused through the entire volume of the test chamber. Also, the molar volume of an ideal gas is considered as 22.4 L, then the analyte concentration in ppm can be computed using the equation given below (Pandeeswari and Jeyaprakash 2014).

The concentration of target gas (ppm), C is given by the following equation:

$$C = \left(\frac{\eta}{V_{chamber}} \right) \times \left(22.4 \frac{L}{mol} \right) \times 10^6, \tag{9}$$

where η is the number of moles of the target analyte in a litre, $V_{chamber}$ is the volume of the test chamber. So the minimum detectable concentration in ppm for 2 µl of target VOCs calculated and found to be 3 ppm, since 3-Carene and α-Pinene have molecular weights 136.24 g/mol and 136.23 g/mol, respectively. The room temperature 3-Carene and α-Pinene sensing response of protonic acid doped polyaniline and polyaniline-WO$_3$ nanocomposite based sensors for 3 ppm concentration is shown in Fig. 14. The 15% WO$_3$ doped polyaniline nanocomposite has shown a good sensitivity towards the target VOCs, compared to the other nanocomposites used. The resistance of all the polyaniline-WO$_3$ nanocomposite material found to be increasing on exposure to the target VOCs inside the test chamber. When the protonic acid doped polyaniline composite gets exposed to the target VOCs, the target analyte molecules pull out the protons from the protonated polyaniline, and due to that the emeraldine state of the polyaniline gets reduced to an intrinsic emeraldine base state, hence the resistance increases. Whereas, when the sensor is brought back to air exposure the process gets reversed, and due to that resistance increases
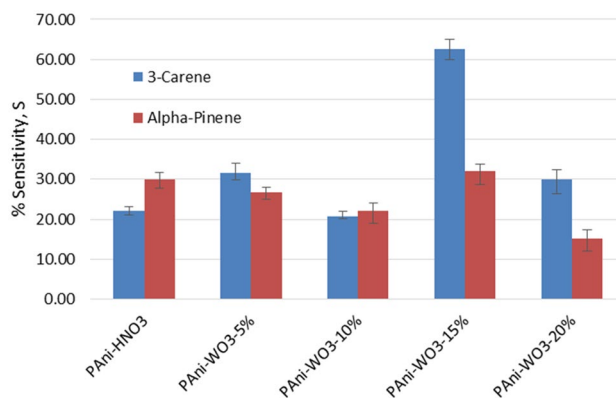
(Bai et al. 2016). Protonic acid doped polyaniline has the minimum sensitivity due to its low surface area and low adsorption of the VOC molecules. The sensitivity of polyaniline-WO$_3$ nanocomposites were found to be increased as the doping concentration of WO$_3$ in polyaniline increased. The maximum sensitivity is found for the nanocomposite containing 15% of WO$_3$. The morphology studies of the 15%-WO$_3$ doped polyaniline nanocomposite shows that the WO$_3$ particles are distributed inside and on the surface of the polyaniline matrix with a sheet structure with a large surface area.

This large surface area is beneficial to adsorption and diffusion of the target analyte molecules on the surface of polyaniline-WO$_3$-15% nanocomposite to achieve a higher sensitivity. Also, this can be due to the p–n heterojunction formed among the p-type HNO$_3$ doped polyaniline and n-type WO$_3$ nanoparticles (Wang et al. 2014). Protonation of polyaniline produces free holes present in the valence band of the composite, while the conduction band of n-type WO$_3$ consists of a huge number of free electrons. So when these WO$_3$ nanoparticles are covered by protonated polyaniline matrix, the electrons and holes will get diffused and form a narrow depletion region at the heterojunction in the equilibrium state. On exposure to the target VOCs, the junction will lose the equilibrium, because the VOC will take out protons from the polyaniline matrix and this will result in the increase in resistance (Tai et al. 2007). Also due to this the depletion region width will increase and this results in narrowing of the conduction channel. So the formation of p–n heterojunction in the polyaniline-WO$_3$ composite with doping concentration 15% exceptionally aids in good sensitivity. The response and recovery curves of polyaniline-WO$_3$-15% nanocomposite for the sensing of VOCs, 3-Carene, and α-Pinene, for concentrations of 3 ppm, 6 ppm and 9 ppm at room temperature is shown in Fig. 15. The resistance of the sensor found to be increasing on exposure with the
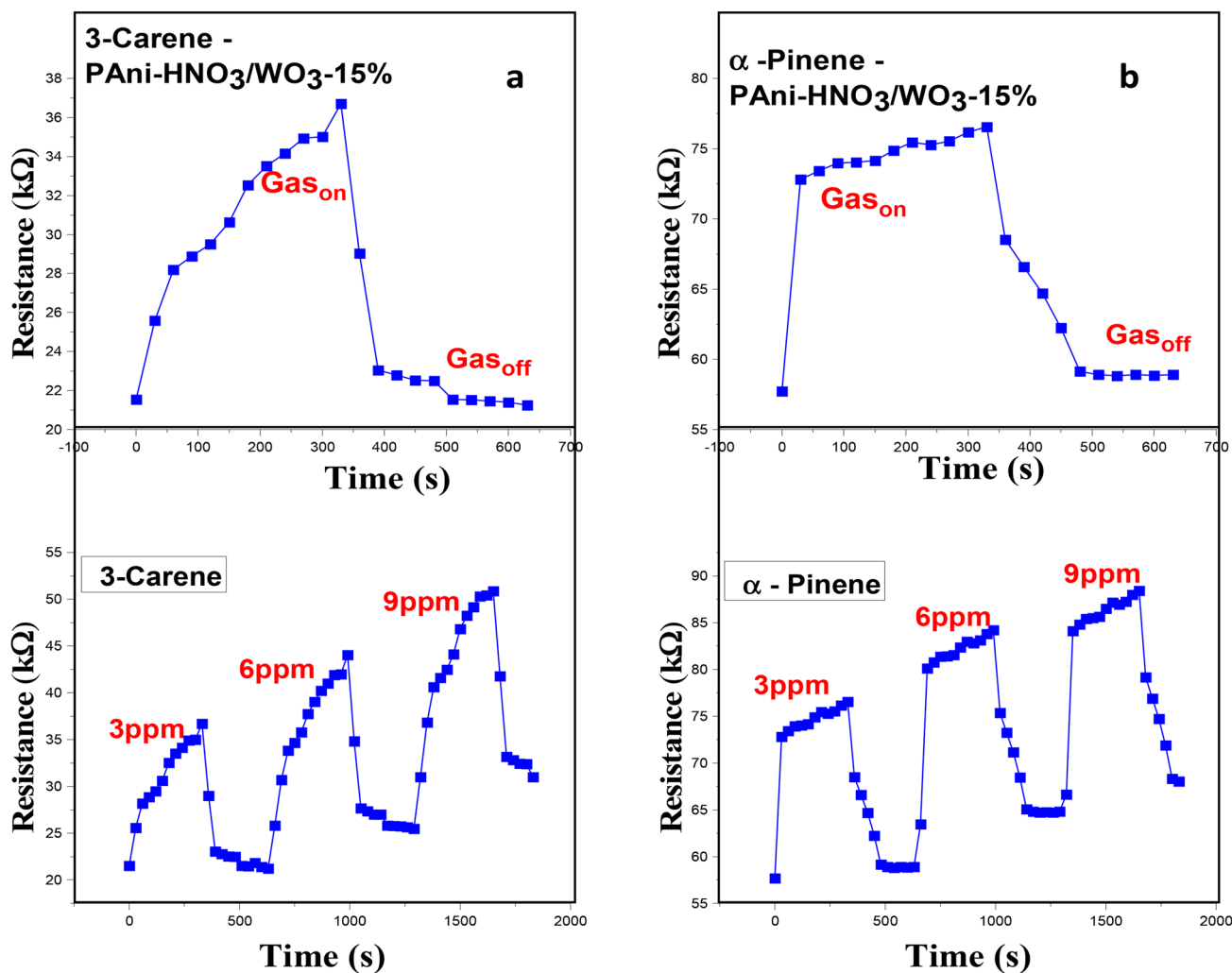
Fig. 15 Response and recovery curves of PAni—HNO$_3$/WO$_3$-15% nanocomposite sensor for VOC: **a** 3-Carene, **b** α-Pinene

target VOC and hence the sensitivity also increased with an increase in concentration of the 3-Carene and α-Pinene. The gas sensitivity percentage of the composites also increased on an increase in gas concentration from 3 to 9 ppm. The response and recovery time calculated from the response curve for 3-carene sensing by the polyaniline-WO$_3$-15% nanocomposite is found to be 135 s and 28 s, respectively. Also, the response time and recovery time for α-Pinene sensing is 7 s and 50 s, respectively. The sensor parameters are found to be better than the previously reported values. The repeated exposure of the VOCs on the same sensor have shown a slight decrease the sensitivity and a smaller increase in the recovery time for the polyaniline-WO$_3$-15% nanocomposite. The sensitivity of polyaniline-WO$_3$ nanocomposite with 15% doping concentration is double than that of protonic acid doped polyaniline, which indicates that polyaniline-WO$_3$-15% nanocomposite is a promising sensing material for the detection malaria based biomarker VOCs,

3-Carene and α-Pinene, at room temperature. To check the selectivity parameter of the sensor, a trial was made to check the sensitivity of the sensor towards the target VOCs among other gases. The selective sensor response is plotted and shown in Fig. 16. The sensitivity for the VOCs acetone and ethanol found to be much lower than that of the sensitivities for 3-Carene and α-Pinene, at room temperature. This indicates that polyaniline-WO$_3$-15% nanocomposite can be used for making breath sensor-based real-time test equipments for malaria detection. The stability of the sensor was checked by measuring its resistance in the air for continuous 7 days at room temperature and the result is shown in Fig. 17. For the first 3 days, the resistance was almost stable, and after there was an increment resistance of the coating and small decline in the sensitivity of the sensor which can be due to the vanishing of unstable adsorption sites (Gaikwad et al. 2017). The response of polyaniline-WO$_3$-15% nanocomposite has shown an instability due to this and it should be
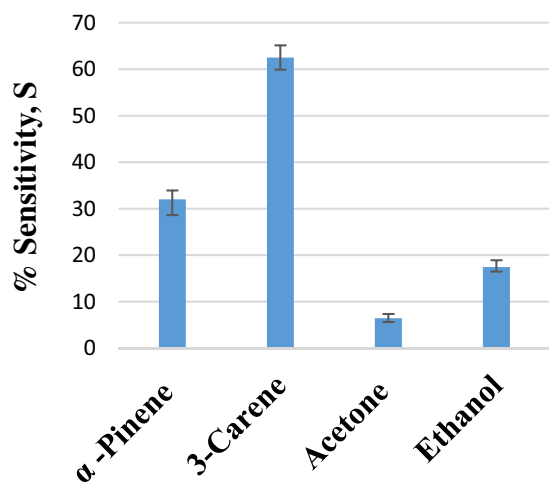
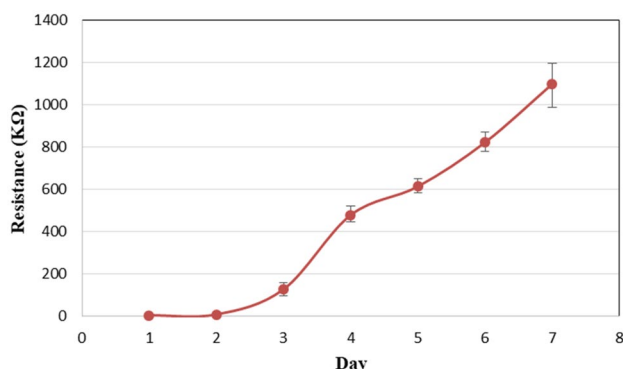Fig. 16 Selectivity of PAni—HNO$_3$/WO$_3$-15% nanocomposite sensor

Fig. 17 Stability of PAni—HNO$_3$/WO$_3$-15% nanocomposite sensor

rectified to achieve better stability for the sensor. Therefore, further studies have to be done to ensure the stability of the nanocomposite to use it as a commercial sensor.

Thermogravimetric analysis

The TGA curves of HNO$_3$ doped polyaniline and its WO$_3$ doped nanocomposites with doping concentrations of 5, 10, 15, and 20 weight percentages, respectively, are shown in Fig. 18. All samples exhibited two major regions of weight loss in the TGA curves. The small weight loss at room temperature to 225 °C is corresponding to the removal of the water content in the samples.

The significant weight loss regions of all the nanocomposites from 225° to 700 °C is due to the decomposition of polyaniline. Due to the introduction of WO$_3$ nanoparticles in various doping concentrations, the weight loss temperature increases from 246.9 °C (HNO$_3$ doped polyaniline) to 253.9, 307.6, 368.9 and 377.2 °C for the polyaniline-WO$_3$ nanocomposite with a filler loading of 5, 10, 15 and 20
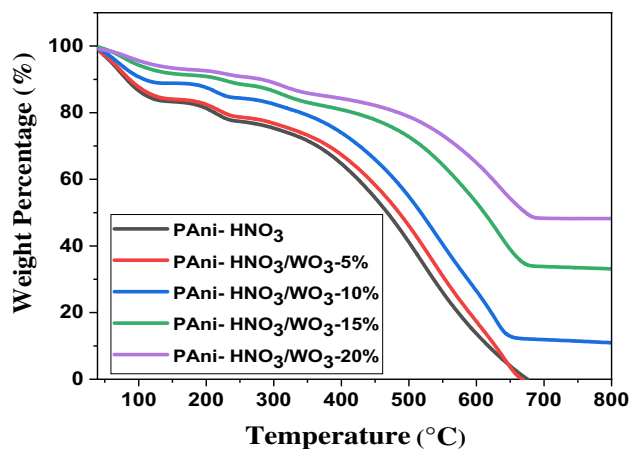

Fig. 18 TGA curves of polyaniline-WO$_3$ nanocomposites

weight%, respectively. Though previous works demonstrate the reduced thermal stability of polyaniline polymer nanocomposites with the addition of inorganic fillers because of the weakened interfacial interaction among the components (Ng and Kasi 2018).In this work, the thermal stability of the polymer nanocomposite is increased, because the protonic acid doped polyaniline matrix closely binds the WO$_3$ nanoparticles to the surface. The compact structure of WO$_3$ nanoparticles in the polymer matrix can help in achieving a higher thermal stability for the polymer nanocomposites (Zhu et al. 2010). The weight remnant of the polymer nanocomposite is higher compared to the mass fraction of the HNO$_3$ doped polyaniline residue. Weight residues of 13.7, 18.9, 44.7, and 57.8% are obtained for the polyaniline polymer nanocomposites doped with 5, 10, 15, and 20 weight% of WO$_3$, respectively. The polymer nanocomposites have larger weight residue compared to the initial particle loading estimation. This is because of the lower monomer conversion in the course of polymerization of aniline, same characteristics are noticed in a SiC/polypyrrole polymer nanocomposite (Mavinakuli et al. 2010).

Conclusions

A 3-Carene and α-Pinene chemiresistive sensor based on polyaniline-WO$_3$ nanocomposite on the FR4 substrate was successfully developed by the in situ chemical polymerization method. Morphological characterization using FESEM and EDAX of the material synthesized confirmed the non-uniform distribution of the WO$_3$ nanoparticles below and above the sheet-like polyaniline matrix. The average crystal-line size, dislocation density, microstrain and Interchain separation length of the polyaniline-WO$_3$ nanocomposites were calculated from the XRD spectra obtained. The chemical structure and bonds present in nanocomposite were analyzed

using FTIR analysis. Transport studies were done using AC conductivity, DC conductivity, and dielectric studies. The characterization results revealed that polyaniline-WO$_3$ nanocomposite with a doping concentration of 15% is the best among the prepared nanocomposites and all the sensing studies were made using the polyaniline-WO$_3$-15% at room temperature with a minimum detection limit of 3 ppm. The sensing layer fabricated using polyaniline-WO$_3$-15% exhibits good sensitivity, better selectivity, reproducibility, fast response and recovery time. The sensor was more selective to 3-Carene and α-Pinene among acetone and ethanol. The fabricated shows an improved sensitivity of 62.49% for the VOC, 3-Carene, and 31.99% for the α-Pinene VOC at room temperature. The resistance of the prepared sensing layer found to be increasing with the number of days of storage. So this stability issue has to be addressed to obtain constant sensitivity for a longer period. The thermal analysis using TGA reveals that the thermal stability of the polyaniline-WO$_3$ nanocomposite is significantly improved due to the introduction of WO$_3$ nanoparticles. From characterizations and sensing studies, it can be concluded that the sensor fabricated using polyaniline-WO$_3$-15% nanocomposite can be a competent candidate for the sensing of malaria biomarker VOCs, 3-Carene and α-Pinene, at room temperature.

Compliance with ethical standards

Conflict of interest On behalf of all authors, the corresponding author states that there is no conflict of interest.

Ethical standard This article does not contain any studies with human or animal subjects.

References

Alfano B, Massera E, Maria A De (2015) Polyaniline proton doping for sensor application, (286998). doi: 10.1109/AISEM.2015.7066824.

Amir A et al (2018) Diagnostic tools in childhood malaria. Parasites Vectors 2018:1–12. https://doi.org/10.1186/s13071-018-2617-y

Aronggaowa B, Kawasaki M, Shimomura T (2013) Thin, transparent conductive films fabricated from conducting polymer nanofibers. Polym J Nat Publ Group 45(8):819–823. https://doi.org/10.1038/pj.2012.214

B CP et al (2010) Electrical resistance response of polyaniline films to water, ethanol, and nitric acid solution *. Chin Phys B 19(8):1–6

Baharuddin AA et al (2019) Materials science in semiconductor processing advances in chemiresistive sensors for acetone gas detection. Mater Sci Semicond Process 103:104616. https://doi.org/10.1016/j.mssp.2019.104616

Bai S et al (2016) Polyaniline @ SnO$_2$ heterojunction loading on flexible PET thin film for detection of NH$_3$ at room temperature.

Sens Actuators: B Chem 226:540–547. https://doi.org/10.1016/j.snb.2015.12.007

Bekri-abbes I, Srasra E (2015) Electrical and dielectric properties of polyaniline and polyaniline/montmorillonite nanocomposite prepared by solid reaction using spectroscopy impedance. J Nanomater 2015:1–8. https://doi.org/10.1155/2015/516902

Berna AZ et al (2015) Analysis of breath specimens for biomarkers of Plasmodium falciparum infection. J Infect Dis 212(7):1120–1128. https://doi.org/10.1093/infdis/jiv176

Bhadra S, Lee JH (2009) Synthesis of higher soluble nanostructured polyaniline by vapor-phase polymerization and determination of its crystal structure. J Appl Polym Sci. https://doi.org/10.1002/app

Bisquert J (2004) Interpretation of AC conductivity of lightly doped conducting polymers in terms of hopping conduction *. Russian J Electrochem. https://doi.org/10.1023/B:RUEL.0000019676.99599.bc

Cao W, Gerhardt R (1990) Calculation of various relaxation times and conductivity for a single dielectric relaxation process. Solid State Ionics 42(3–4):213–221

Devi MR et al (2019) Fabrication, spectral characterization, XRD and SEM studies on some organic acids doped polyaniline thin films on glass substrate. J King Saud Univ Sci 31(4):1290–1296. https://doi.org/10.1016/j.jksus.2018.02.008

Dhivya C, Vandarkuzhali SAA, Radha N (2016) Antimicrobial activities of nanostructured polyanilines doped with aromatic nitro compounds. Arab J Chem King Saud Univ. https://doi.org/10.1016/j.arabjc.2015.12.005

Du X et al (2014) Polyaniline with high crystallinity degree: synthesis structure, and electrochemical properties. J Appl Polym Sci 40827:6–13. https://doi.org/10.1002/app.40827

Gaikwad G et al (2017) Synthesis and evaluation of gas sensing properties of PANI based graphene oxide nanocomposites. Mater Sci Eng B 218:14–22. https://doi.org/10.1016/j.mseb.2017.01.008

Gomathi M, Rajkumar PV, Prakasam A (2018) Results in physics study of dislocation density (defects such as Ag vacancies and interstitials) of silver nanoparticles, green-synthesized using Barleria cristata leaf extract and the impact of defects on the antibacterial activity. Results Phys 10:858–864. https://doi.org/10.1016/j.rinp.2018.08.011

Hawari HF et al (2013) Highly selective molecular imprinted polymer (MIP) based sensor array using interdigitated electrode (IDE) platform for detection of mango ripeness. Sens Actuators: B Chem 2013:1–11. https://doi.org/10.1016/j.snb.2013.01.045

Ho CK, Laboratories SN (2015) Review of chemical sensors for in-situ monitoring of volatile contaminants. Sandia Rep. https://doi.org/10.2172/780299

Hua B (2014) Gas sensors based on conducting polymers. Sensors. https://doi.org/10.3390/s7030267

Huang T et al (2018) Fabrication of rigid and flexible SrGe$_4$O$_9$ nanotube-based sensors for room-temperature ammonia detection. Nano Res 11(1):431–439. https://doi.org/10.1007/s12274-017-1650-z

Jin L et al (2016) High-resolution p-type metal oxide semiconductor nanowire array as an ultrasensitive sensor for volatile organic compounds. Nano Lett. https://doi.org/10.1021/acs.nanolett.6b01713

Kadosaki M et al (2010) Development of an oxide semiconductor thick film gas sensor for the detection of total volatile organic compounds. Electron Commun Jpn 93(10):125–130. https://doi.org/10.1002/ecj.10190

Kang ET, Neoh KG, Tan KL (1993) Polyaniline with high intrinsic oxidation state. Surf Interface Anal 20(10):833–840. https://doi.org/10.1002/sia.740201006

Kar P, Choudhury A (2012) Electrical and dielectric properties of polyaniline doped with carboxyl-functionalized multiwalled carbon

nanotube. Adv Polym Technol 32(2013):760–770. https://doi.org/10.1002/adv

Kellenberger A, Dmitrieva E, Dunsch L (2012) Structure dependence of charged states in " Linear " polyaniline as studied by in situ ATR-FTIR spectroelectrochemistry. J Phys Chem B 116(14):4377–4385

Kelly M et al (2015) Malaria parasites produce volatile mosquito attractants. MBio 6(2):1–6. https://doi.org/10.1128/mBio.00235-15.Editor

Kumar N et al (2002) Studies on conductivity and dielectric properties of polyaniline–zinc sulfide composites. Bull Mater Sci 29(4):379–384

Laslau C et al (2009) Morphological evolution of self-assembled polyaniline nanostructures obtained by pH-stat chemical oxidation. Chem Mater 21(5):954–962

Lee SP (2015) Terpene sensor array with bridge-type resistors by CMOS technology. IOP Conf Ser: Mater Sci Eng 87(1). doi: 10.1088/1757-899X/87/1/012065.

Lee S et al (2012) Massive po&arons in large-energy-gap polymers. J Chem Inf Model 53(9):1689–1699. https://doi.org/10.1017/CBO9781107415324.004

Mavinakuli P et al (2010) Polypyrrole/silicon carbide nanocomposites with tunable electrical conductivity. J Phys Chem C 114:3874–3882

Menard D, Dondorp A (2017) Antimalarial drug resistance: a threat to malaria elimination. Cold Spring Harbor Perspect Med, 2009.

Metals ES (1994) 'Im|TIS The concept of secondary doping as applied to polyaniline. Synth Metals 65:103–116

Mote VD, Purushotham Y, Dole BN (2012) Williamson-Hall analysis in estimation of lattice strain in nanometer-sized ZnO particles. J Theor Appl Phys 2012:2–9

Moyeh MN et al (2019) Comparison of the accuracy of four malaria diagnostic methods in a high transmission setting in coastal Cameroon. J Parasitol Res, 2019.

Ng HM, Kasi R (2018) Thermogravimetric analysis of polymers. Encycl Polym Sci Technol. https://doi.org/10.1002/0471440264.pst667

Pandeeswari R, Jeyaprakash BG (2014) High sensing response of β-Ga$_2$O$_3$ thin film towards ammonia vapours: influencing factors at room temperature. Sens Actuators B: Chem 195:206–214. https://doi.org/10.1016/j.snb.2014.01.025

Park SJ, Park CS, Yoon H (2017) Chemo-electrical gas sensors based on conducting polymer hybrids. Polymers. https://doi.org/10.3390/polym9050155

Qasim H et al (2007) Optical and conductivity dependence on doping concentration of polyaniline nanofibers. doi: 10.1117/12.758331.

Sanches EA et al (2011) Structural characterization of emeraldine-salt polyaniline/gold nanoparticles complexes. J Nanomater 2011:1–8. https://doi.org/10.1155/2011/697071

Sastry DN et al (2013) DC conductivity studies of doped polyaniline tungsten oxide nanocomposites. 20: 435–442.

Schaber CL et al (2018) Breathprinting reveals malaria-associated biomarkers and mosquito attractants. J Infect Dis 63110:1553–1560. https://doi.org/10.1093/infdis/jiy072

Sen T, Shimpi NG, Mishra S (2016) Room temperature CO sensing by polyaniline/Co$_3$O$_4$ nanocomposite. J Appl Polym Sci 133(42):4–11. https://doi.org/10.1002/app.44115

Tai H et al (2007) Fabrication and gas sensitivity of polyaniline–titanium dioxide nanocomposite thin film. Sens Actuators B: Chem 125(2):644–650. https://doi.org/10.1016/j.snb.2007.03.013

Tangpukdee, N. et al. (2009) 'Malaria Diagnosis : A Brief Review', 47(2), pp. 93–102. doi: 10.3347/kjp.2009.47.2.93.

Trchová M, Stejskal J (2011) Polyaniline: The infrared spectroscopy of conducting polymer nanotubes (IUPAC Technical Report)*. Pure Appl Chem 83(10):1803–1817. https://doi.org/10.1351/PAC-REP-10-02-01

Wang L et al (2014) Enhanced sensitivity and stability of room-temperature NH$_3$ sensors using core−shell CeO$_2$ nanoparticles @ cross-linked PANI with p–n heterojunctions. ACS Appl Mater Interfaces 6(16):14131–14140

Weerakoon KA, Hiremath N, Chin BA (2012) Polymer-based sensor array for phytochemical detection. Int Soc Opt Photon 8369:1–8. https://doi.org/10.1117/12.920512

World malaria report 2019 (2019).

Zhu J et al (2010) Conductive polypyrrole/tungsten oxide metacomposites with negative permittivity. J Phys Chem C 114:16335–16342

Zou B et al (2014) Tungsten oxide and polyaniline composite fabricated by surfactant-templated electrodeposition and its use in supercapacitors, 2014.